Sawtooth oscillations in a damped/driven cryogenic electron plasma: Experiment and theory

B. P. Cluggish,[a] C. F. Driscoll, K. Avinash,[b] and J. A. Helffrich[c]

Department of Physics, 0319, University of California at San Diego, La Jolla, California 92093

Measurements have been made of nonlinear sawtooth oscillations of the displacement of a magnetized electron column in a cryogenic, cylindrical trap. First reported 7 years ago, these oscillations occur when the displacement is destabilized by a resistive wall and damped by a temperature-dependent collisional viscosity. A typical evolution can last for thousands of seconds. Measurements show that oscillations of the plasma displacement are accompanied by oscillations in the plasma temperature. A simple predator-and-prey model of the temperature and displacement gives rise to a limit cycle solution due to the nonmonotonic dependence of the viscosity on temperature. These limit cycles are in good quantitative agreement with the measured sawtooth oscillations. © *1997 American Institute of Physics.* [S1070-664X(97)01305-0]

I. INTRODUCTION

Nonlinear relaxation oscillations are a common phenomenon in plasma physics. Examples include the sawtooth instability,[1] fishbone oscillations,[2] and edge localized modes[3] (ELM's) in confined fusion plasmas, and the potential relaxation instability in Q-machines[4] and discharges.[5] These oscillations are often modeled by predator-and-prey equations[6] where one parameter "preys" on another, resulting in a nonlinear coupling between the rates of change of the two quantities.

In this paper, we present measurements of a complex, nonlinear evolution of the displacement and temperature of a magnetized electron column in a cylindrical trap. First reported 7 years ago,[7] this behavior occurs when the displacement is destabilized by a resistive wall and damped by a temperature-dependent collisional viscosity. A typical evolution can last for thousands of seconds. In addition to nonlinear sawtooth oscillations, we observe linear oscillations, quiescent periods where the displacement is nearly constant, and bifurcation between these phenomena. Measurements show that oscillations of the plasma displacement are accompanied by oscillations in the plasma temperature. Furthermore, the radius of the plasma column increases much more rapidly than when the plasma is centered in the trap.

We find that a simple model quantitatively reproduces the nonlinear behavior of the displacement, temperature, and plasma radius. In this model, the coupling between the three variables is due to the relatively well-understood transport and heating process called "rotational pumping."[8] Rotational pumping is the collisional dissipation of the axial compressions which are caused by $\mathbf{E} \times \mathbf{B}$ rotation of the column through asymmetric confinement potentials; here, the confinement potentials appear asymmetric only because of the displacement of the column away from the symmetry axis of the trap. Rotational pumping simultaneously decreases the plasma displacement, increases the plasma radius, and Joule-heats the plasma.

In the limit where the plasma radius changes relatively slowly, the evolution of the displacement and temperature is described by a pair of predator-and-prey equations, in which the plasma radius is a control parameter. In this limit, equilibrium points can be found where the resistive growth of the displacement is balanced by rotational pumping damping, and the cooling of the plasma through cyclotron radiation is balanced by Joule-heating. The locations of the equilibrium points depend on the plasma radius, while the stability of these equilibria is determined by the dependence of rotational pumping transport on temperature.

The complex behavior of the plasma arises because the rotational pumping transport rate γ has a nonmonotonic dependence on temperature T. As shown in Fig. 1, the measured $\gamma(T)$ is peaked at about 0.1 eV. The solid curve is the theoretical prediction of the transport rate. The Joule-heating rate is proportional to γ and to the square of the displacement D, while the cyclotron radiation cooling rate is proportional to T. The equilibrium temperature is stable above about 0.02 eV, where the slope of the cooling rate with respect to T is steeper than that of the heating rate. Any increase (decrease) in T increases (decreases) the cooling rate more than the heating rate, restoring the equilibrium temperature.

Sawtooth oscillations occur when the equilibrium temperature is in the unstable region below about 0.02 eV, where the heating rate has the steeper slope. Any small decrease in T then decreases the heating rate more than the cooling rate, causing a rapid cooling of the plasma until the temperature reaches a minimum set by Joule-heating from background transport. However, the corresponding decrease in the damping rate γ subsequently allows D to grow until the heating rate exceeds the cooling rate even at the minimum temperature. The temperature then unstably grows until it reaches a new, quasi-stable equilibrium near the peak in Fig. 1. Now, γ is relatively large, causing D to slowly diminish until the cooling rate exceeds the heating rate at all temperatures. The temperature then unstably decreases back
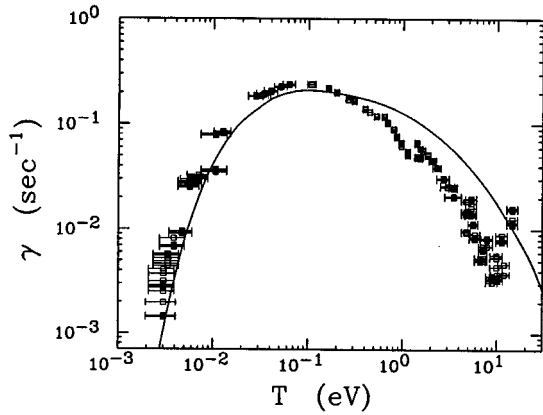
FIG. 1. Dependence of the rotational pumping transport and damping rate, γ, on plasma temperature T. The data points are measured values. The solid curve is the prediction of the rotational pumping theory when the three-dimensional plasma shape is numerically calculated from the measured density profile. The Joule-heating rate is proportional to γD^2.

FIG. 3. Schematic of a cross sectional view of the apparatus, with the plasma drifting around the trap axis at a displacement D in an $m=1$ diocotron orbit. The plasma simultaneously rotates around its own axis at a frequency f_E. The wall sectors are electrically isolated from the grounded wall.

to the minimum temperature, from whence the next sawtooth oscillation begins.

II. EXPERIMENTAL APPARATUS

We confine the electron plasmas in a Penning–Malmberg trap,[9,10] shown schematically in Fig. 2. Electrons emitted from a tungsten filament are confined in a series of conducting cylinders of radius $R_w = 1.27$ cm, enclosed in a vacuum can at 4.2 K. The electrons are confined axially by negative voltages $V_c = -200$ V on cylinders 1 and 4; radial confinement is provided by a uniform axial magnetic field, with $40 < B < 60$ kG. The trapped plasma typically has initial density $10^9 \leq n \leq 10^{10}$ cm^{-3}, radius $R_p \sim 0.06$ cm, length $L_p \sim 3$ cm, with a characteristic radial expansion time $10^2 < \tau_m < 10^3$ s. The apparatus is operated in an inject/manipulate/dump cycle, and has a shot-to-shot reproducibility of $\delta n/n \sim 1\%$.

The self electric field of the electrons causes an $\mathbf{E} \times \mathbf{B}$ drift rotation around an axis through the center of charge, at a rate $0.3 \leq f_E \leq 3$ MHz. This rotation rate tends to be less than the axial bounce frequency for a thermal electron, with $0.4 \leq f_b \leq 40$ MHz for $0.001 < T < 10$ eV.
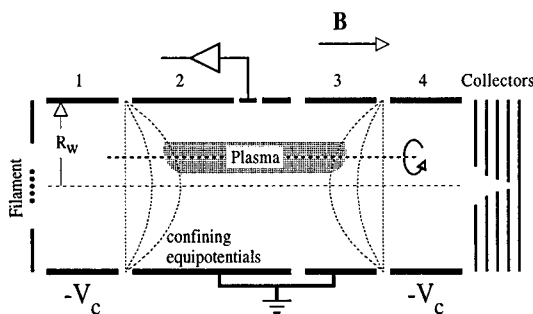

FIG. 2. Schematic of the cylindrical apparatus and electron plasma. The curvature of the confining equipotentials causes the distortion of the shape of the plasma ends, resulting in rotational pumping transport and damping.
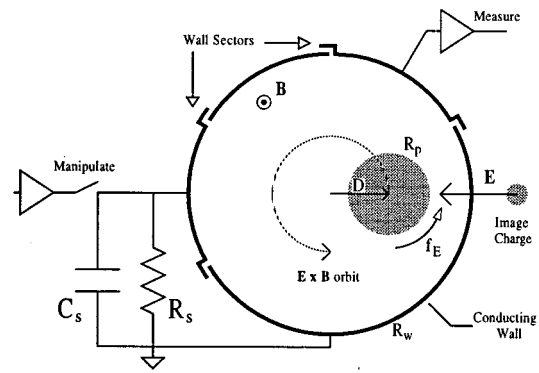
When the plasma is centered in the trap, the z-integrated density or temperature of the plasma can be measured by dumping the electrons onto the end collectors, by grounding cylinder 4. A rough histogram of the z-integrated density is obtained from the charge on the 5 collectors. We smooth out this histogram by fitting it to a z-integrated density profile of the form $Q(r) \propto \exp(-(r/a)^p)$, where a and p are free parameters. While there is no a priori reason for the density profile to have this form, more careful measurements of the density profile have shown it to be a reasonable approximation. Also, for the purposes of this paper, we are only interested in the mean plasma radius, which is insensitive to the detailed form of the profile. We define the plasma radius by

$$R_p \equiv \frac{3}{2} \frac{\int_0^{R_w} r^2 \, dr \int n \, dz}{\int_0^{R_w} r \, dr \int n \, dz}. \tag{1}$$

For a plasma with uniform density out to R_0, this gives $R_p = R_0$.

The parallel plasma temperature, $T_\parallel$, is measured by slowly ramping the voltage on cylinder 4 to ground, and measuring the number of electrons which escape as a function of the confining voltage. We can reproducibly create plasmas with $0.001 \leq T_\parallel \leq 20$ eV, which gives $T_\parallel$ to $T_\perp$ collisional equilibration rates $10^3 \leq \nu_{\perp\parallel} \leq 10^5$ s^{-1}.

We calculate the z-dependent plasma density $n(r,z)$ and space charge potential $\phi(r,z)$ from the measured z-integrated charge $Q(r)$ and $T_\parallel$, by numerically solving Poisson's equation, assuming that the electrons are in local thermal equilibrium along each field line. That is, we assume

$$n(r,z) = n_0(r)\exp\{e\phi(r,z)/kT_\parallel\}, \tag{2}$$

where $n_0(r)$ is obtained by requiring that $\int n(r,z)dz = Q(r)$.

The electrons cool by cyclotron radiation. At $B = 40$ kG, the measured radiative cooling time is $\tau_{rad} = 0.29$ s.[9] Because $\tau_{rad} \gg \nu_{\perp\parallel}^{-1}$, the perpendicular and parallel temperatures are presumed to be nearly equal, i.e., $T_\perp \approx T_\parallel \approx T$.

Figure 3 shows a cross-sectional view of the trap, with

the magnetic field out of the page. A plasma column which is displaced from the axis of the trap will $\mathbf{E} \times \mathbf{B}$ drift around the trap axis due to the electric field of its image charge. This center of mass orbit is called the $m=1$ diocotron mode, and has linear mode frequency $f_D = N_L e c / \pi B R_w^2$, where D is the displacement of the plasma column from the axis of the trap, and N_L is the number of electrons per unit length of the column. Also, there are small nonlinear and finite length corrections to f_D depending on D/R_W, R_p/R_w, and L_p/R_p.[11] In our experiments, $5 < f_D < 20$ kHz, so the orbit frequency is always small compared to the plasma rotation frequency, i.e., $f_D \ll f_E$.

The diocotron mode is detected by using one of 2 electrically isolated wall sectors. The amplitude of the image charge current induced in the wall sector by the diocotron mode is proportional to D and N_L. Since N_L is nearly constant as the plasma evolves, we can measure the evolution of D nondestructively.

The diocotron mode is manipulated using the other wall sector. The mode is initially induced by pulsing the sector to a negative voltage for one-half a mode period, which causes the column to $\mathbf{E} \times \mathbf{B}$ drift away from the trap axis. Later, negative feedback[12] from the detecting sector to the transmitting sector is used to move the plasma back to the trap axis before dumping, in order to measure the density or temperature.

In the experiments presented in this paper, the diocotron mode is continually destabilized by a resistance R_s which is attached to the wall sector. The flow of the image charge current through the resistor dissipates the mode energy. This causes the displacement to increase since the diocotron mode is a negative energy mode; the mode energy decreases as the plasma approaches its image charge. In the absence of damping, the displacement D grows exponentially at a rate β, which we call the resistive growth rate.[13] For a long plasma, β is given by

$$\beta = \frac{L_s^2 \sin^2(\theta_s/2)}{\pi^2 L_p R_s C_s^2} \frac{(2\pi f_D R_s C_s)^2}{1 + (2\pi f_D R_s C_s)^2}, \quad (3)$$

where L_s and θ_s are the axial and azimuthal dimensions of the wall sector, and $R_s - i/2\pi f_D C_s$ is the impedance between the sector probe and the grounded wall. In our experiments, $R_s \approx 50$ kΩ, and $C_s \approx 400$ pF, giving typical growth rates $\beta \sim 0.1$ s^{-1}. Note that since f_D depends only weakly on the shape of the density profile, β remains nearly constant as the plasma evolves.

III. ROTATIONAL PUMPING

The plasmas in our experiments are subject to continual rotational pumping transport,[8,10] which damps the diocotron mode, increases the plasma radius, and heats the plasma. This transport occurs because the confining equipotential surfaces are curved, as shown in Fig. 2. This causes axial compressions in a plasma which is displaced from the trap axis, due to the rotation of the plasma around its own axis. The plasma heats due to the dissipation of these compressions by the collisional, compressional viscosity of the plasma. Conservation of energy then requires the plasma to
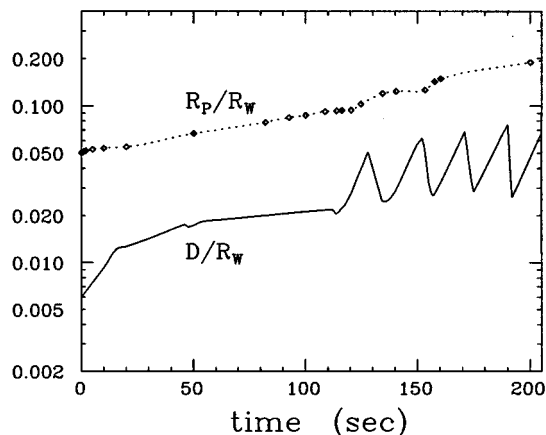

FIG. 4. Typical measured evolution of the plasma radius R_p and displacement D (scaled by the wall radius R_w), when a 30 kΩ resistor destabilizes the $m=1$ diocotron mode. The evolution of D is measured in one shot, while the evolution of R_p is built up over many shots.

decrease in electrostatic energy by expanding radially as its thermal energy increases. Likewise, conservation of angular momentum requires the plasma to move back to the trap axis as it expands.

For a uniform density and temperature plasma, an estimate of the rotational pumping damping rate of the diocotron mode, γ_{est}, is given by

$$\gamma_{\text{est}} = 2\kappa^2 \nu_{\perp\parallel} \left(\frac{\lambda_D}{L_p}\right)^2 \frac{(R_p/R_w)^2}{1 - (R_p/R_w)^2}. \quad (4)$$

Here, $\lambda_D = (kT/4\pi e^2 n)^{1/2}$ is the Debye length and κ characterizes the geometry of the axial compressions. For $\lambda_D \ll R_p$, numerical calculations of realistic end shapes give $\kappa^2 \approx 2.25 R_w/R_p$.[10] The estimate of Eq. (4) can be further improved by calculating the three-dimensional shape of the plasma,[10] and by numerically integrating the rotational pumping theory[14] over the measured plasma profile $n(r)$. This gives the solid curve of Fig. 1, which is close to the measured rates.

IV. EXPERIMENTAL OBSERVATIONS

Figure 4 shows a typical evolution of the plasma displacements D and radius R_p when D is resistively destabilized. Here, $R_s = 30$ kΩ, $B = 50$ kG, and the initial density is $n = 8.6 \times 10^9$ cm^{-3}. The displacement is given a small, nonzero value immediately after injection in order to ''seed'' the resistive growth instability. Initially, D increases exponentially with time. However, after about 20 s, the resistive growth appears to saturate. A quiescent period follows, during which D changes only slowly. At 110 s, there is a bifurcation into sawtooth oscillations, which have a period of about 20 s. These sawtooth oscillations can last for thousands of seconds. Concurrent with this evolution of the displacement is a continual increase in the plasma radius, at a rate much larger than is observed for a plasma which remains on axis. However, no temperature measurements were made for this evolution because such measurements are exceedingly time consuming for long confinement times.
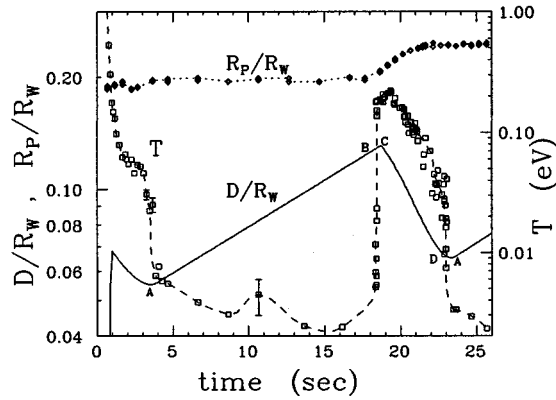
FIG. 5. Typical measured evolution of D, R_p, and the temperature T during one sawtooth oscillation. The left ordinate corresponds to D and R_p, the right to T. Typical error bars for T are shown. The sawtooth "crash" in D is preceded by a sharp rise in T. Similarly, the sawtooth "rise" in D is preceded by a sharp drop in T. The plasma radius grows only during the sawtooth crashes.

Measurements of shorter evolutions show that the sawtooth oscillations in D are coupled to oscillations in the temperature T, and that each sawtooth crash is accompanied by an increase in the plasma radius R_p. Figure 5 shows the evolution of the plasma displacement, temperature, and radius during a single sawtooth oscillation. The left ordinate corresponds to D and R_p, and the right to T. Here, $R_s = 47$ kΩ, $B = 60$ kG, and the initial density is 6.0×10^8 cm^{-3}. The plasma temperature is $T \approx 1$ eV at injection, but it rapidly cools down to $T \approx 0.003$ eV at the beginning of the sawtooth oscillation at $t = 3.5$ s. During the rising period of the sawtooth, D grows exponentially with time, but T and R_p remain nearly constant. However, at $t = 18.4$ s, T rapidly increases by a factor of 60 in 0.1 s. The displacement and temperature then decrease for 5 s, during which time the plasma radius increases by 25%. At 23 s, T drops from 0.03 eV to 0.003 eV in about 0.1 s, and the cycle begins again.

In other parameter regimes, we observe small, sinusoidal oscillations of the displacement and temperature. A typical evolution is shown in Fig. 6. Here, $R_s = 30$ kΩ, $B = 40$ kG, and the initial density is 6.3×10^8 cm^{-3}. Again, the plasma is fairly hot upon injection, $T \approx 1$ eV, but it rapidly cools until $t = 6$ s, whereupon T increases with increasing D. By $t = 10$ s, D and T have settled into sinusoidal oscillations with a frequency of about 8.5 s. The phase of the temperature oscillation lags behind the displacement by $\pi/2$. These oscillations are damped, i.e., the oscillation amplitude of the second cycle is smaller than the first for both D and T. In contrast with Fig. 5, here the plasma radius increases slowly and continually over the 25 s evolution. At later times in this evolution, the oscillations grow. Figure 7 shows the evolution of the displacement out to 100 s. The damping of the sinusoidal oscillations continues until the third oscillation. Thereafter, the oscillations grow and then bifurcate into sawtooth oscillations.
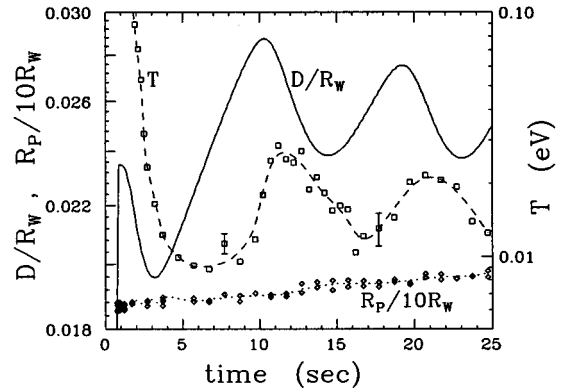

FIG. 6. Typical measured small oscillations of D and T accompanied by a constant slow increase in R_p. The left ordinate corresponds to D and R_p, the right to T. Typical error bars for T are shown. Note that R_p/R_w has been scaled down by a factor of 10 to fit in the plot. The oscillations in D and T are damped; T lags behind D by a phase of $\pi/2$.

V. MODEL EQUATIONS

Figures 5 and 6 show that the oscillations in displacement are coupled to oscillations in temperature. Using a simple model, we show that this coupling arises through rotational pumping transport. We model the plasma using three parameters: the temperature T, the displacement D, and the plasma radius R_p. We assume that the plasma is uniform in density and temperature and is of fixed length. The evolution equations for the three parameters are then

$$\frac{d}{dt}T = \frac{2}{3}N_L e^2\left[2\gamma\frac{D^2}{R_p^2}\left(1 - \left(\frac{R_p}{R_w}\right)^2\right) + \epsilon\right] - \frac{(T - T_w)}{\tau_{\rm rad}}, \quad (5)$$

$$\frac{d}{dt}D = (\beta - \gamma)D, \quad (6)$$

$$\frac{d}{dt}R_p = \left[2\gamma\frac{D^2}{R_p^2} + \epsilon\right]R_p, \quad (7)$$

where β is given by Eq. (3), $\gamma(T, R_p)$ is given by Eq. (4), $T_w = 3.7 \times 10^{-4}$ eV (4.2 K) is the wall temperature, and ϵ is
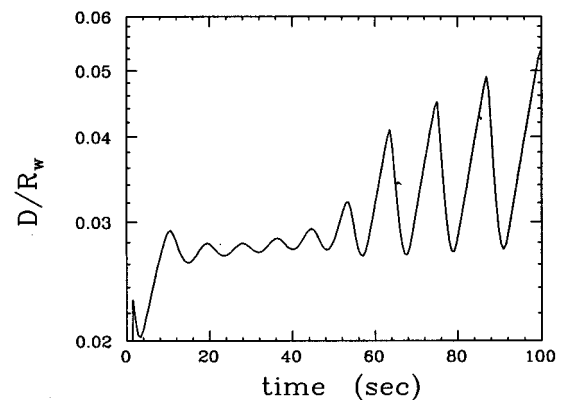

FIG. 7. Long time evolution of D measured under the same conditions as the data shown in Fig. 6. The small oscillations damp for 3 cycles, then grow for 3 cycles before changing into growing sawtooth oscillations.
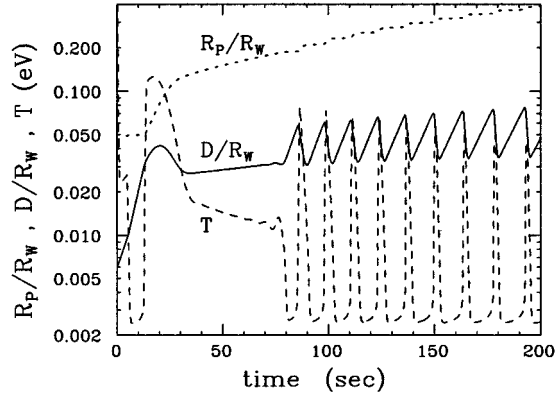
FIG. 8. Model evolution of D, T, and R_p obtained by numerically integrating Eqs. (5)–(7), starting from the same initial conditions as the measured evolution shown in Fig. 4. The evolutions of D and R_p are similar to the measured evolutions, and the coupling between D and T is similar to that shown in the data in Figs. 5–6.

the ''anomalous'' transport rate. (Anomalous transport is the slow expansion of the plasma due to small construction asymmetries in the trap.[15]) In Eqs. (5)–(7), the evolution of D is governed by a competition between resistive growth β and rotational pumping damping γ. Similarly, T evolves due to the competing effects of Joule-heating from rotational pumping and anomalous transport and cooling by cyclotron radiation towards T_w. The displacement and temperature are coupled because the damping rate γ depends on T and the rotational pumping Joule-heating rate is proportional to D^2. The plasma radius increases monotonically due to rotational pumping and anomalous transport.

Figure 8 shows a simulated evolution of D, T, and R_p, obtained by numerically integrating Eqs. (5)–(7), starting from the same initial conditions as the data in Fig. 4. Since anomalous transport is weak and poorly understood, we simply set ϵ equal to a constant value, $\epsilon = 0.0023$ s^{-1}. (This value was obtained from measurements of the transport rate of a plasma identical to that measured for Fig. 4, but with $D=0$ and $R_s=0$.)

The simulation reproduces the same qualitative evolution of D as shown in Fig. 4, with factor-of-2 quantitative agreement. Both Fig. 4 and Fig. 8 show initial linear growth, which saturates and is followed by a quiescent period where D is slowly increasing. The simulation also reproduces the bifurcation into sawtooth oscillations. Examination of the temperature evolution in the simulation shows strong coupling between D and T. During the quiescent period between 32 and 77 s in Fig. 8, the temperature slowly decreases as D slowly increases, while the bifurcation into sawtooth oscillations of D is accompanied by a steep drop in T. In addition, the simulation shows that each sawtooth crash of D is accompanied by a temperature ''spike.'' These temperature oscillations are similar to the observed oscillations shown in Fig. 5. Finally, R_p increases with each sawtooth crash in the simulation, just as in the observed evolution in Fig. 5.

VI. PREDATOR-AND-PREY MODEL

The good agreement between the simulation (Fig. 8) and the data (Fig. 4) indicates that Eqs. (5)–(7) are sufficient to describe the plasma. These equations can be further simplified if we note that R_p changes much more slowly than D or T in Figs. 4–6. In this section, we set $R_p=$ const in Eqs. (5)–(7). We find that most of the observed plasma behavior can be derived analytically in this limit. The magnitude of R_p is found to determine the stability of D and T.

Since R_p is a constant, we set the $m=1$ diocotron mode frequency f_D to be constant, and hence the resistive growth rate β to be constant as well [see Eq. (3)]. Since the simulated evolution shown in Fig. 8 reproduces most of the features of the measured evolution, we keep the approximation $\epsilon=$ const. We can then define a minimum temperature, $T_{\min}$, given by

$$T_{\min} \equiv \frac{2}{3} N_L e^2 \epsilon \tau_{\rm rad} + T_w. \tag{8}$$

$T_{\min}$ is the minimum temperature to which the plasma can cool through cyclotron radiation.

Defining new temperature and displacement variables by

$$\mathscr{T} \equiv \frac{3}{2}(T - T_{\min}),$$

$$\mathscr{D} \equiv 2 N_L e^2 \left(1 - \frac{R_p^2}{R_w^2}\right) \frac{D^2}{R_p^2},$$

we can rewrite Eqs. (5) and (6) as

$$\frac{d}{dt}\mathscr{T} = \gamma \mathscr{D} - \frac{\mathscr{T}}{\tau_{\rm rad}}, \tag{9}$$

$$\frac{d}{dt}\mathscr{D} = 2[\beta - \gamma]\mathscr{D}, \tag{10}$$

where $\gamma \equiv \gamma(\mathscr{T})$. We note that if γ were proportional to $\mathscr{T}$, Eqs. (9) and (10) would be the same as the Lotka–Volterra predator-and-prey equations,[6] with $\mathscr{T}$ and $\mathscr{D}$ being the populations of predators and prey, respectively. Here, Eqs. (9) and (10) are the rates of change of the thermal and electrostatic energies per electron.

A. Fixed points

Equations (9) and (10) have fixed points $(\mathscr{T}_i, \mathscr{D}_i)$, $i=0,1,2$, where $d\mathscr{D}/dt = d\mathscr{T}/dt = 0$. The $i=0$ fixed point is $\mathscr{D}_0 = \mathscr{T}_0 = 0$. The other two are determined by balancing the competing terms in Eqs. (9) and (10). Setting the resistive growth rate equal to the rotational pumping damping rate in Eq. (10) defines two equilibrium temperatures, $\mathscr{T}_1$ and $\mathscr{T}_2$, i.e.

$$\beta = \gamma(\mathscr{T}_i), \qquad i=1,2.$$

Figure 9 shows typical values of β and γ as functions of $\mathscr{T}$. Here we have used $\beta = 0.09$ s^{-1} and $T_{\min} = 0.002$ eV. The damping rate, $\gamma(\mathscr{T})$, is obtained from the theory curve in Fig. 1. There is one $\mathscr{T}_i$ on each side of the peak in γ. Obviously, if β is larger than the peak in γ, there is no equilibrium and $\mathscr{D}$ increases without bound. However, when
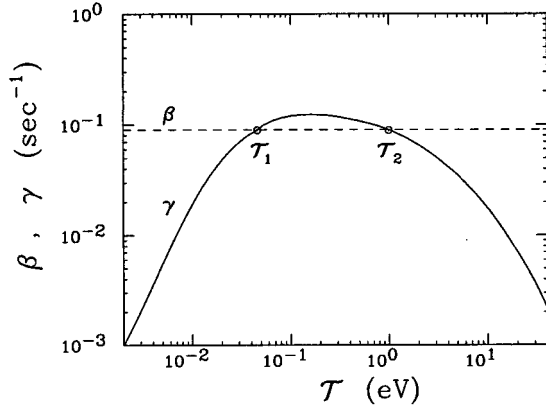
Cluggish et al.

FIG. 9. Calculation of the equilibrium temperatures $\mathcal{T}_1$ and $\mathcal{T}_2$ by setting the resistive growth rate β (dashed line) equal to the damping rate $\gamma(\mathcal{T})$ (solid curve).

$D > R_p$, the assumption that R_p is slowly varying does not hold. The case where R_p is rapidly increasing is discussed in Section VIII.

Setting the Joule-heating rate equal to the cyclotron radiation cooling rate in Eq. (9) with $\mathcal{T} = \mathcal{T}_i$ yields 2 equilibrium displacements, $\mathcal{D}_1$ and $\mathcal{D}_2$:

$$\beta \mathcal{D}_i = \mathcal{T}_i / \tau_{rad}, \qquad i = 1, 2.$$

Figure 10 shows $\beta\mathcal{D}$, $\mathcal{T}_1 / \tau_{rad}$, and $\mathcal{T}_2 / \tau_{rad}$ plotted versus $\mathcal{D}$, with $\tau_{rad} = 0.1$ s. The $\mathcal{D}_i$ are proportional to the $\mathcal{T}_i$.

B. Stability

The stability of the 3 equilibria is determined by linearizing Eqs. (9) and (10) around the 3 fixed points. We define, for $i = 0, 1, 2$,

$$\delta \mathcal{T}_i = \mathcal{T} - \mathcal{T}_i,$$

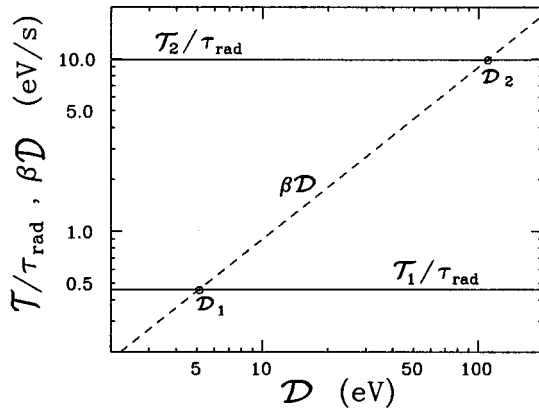$$\delta \mathcal{D}_i = \mathcal{D} - \mathcal{D}_i,$$

FIG. 10. Calculation of the equilibrium displacements $\mathcal{D}_1$ and $\mathcal{D}_2$ by setting the Joule-heating rate $\gamma\mathcal{D}$ (dashed line) equal to the cyclotron radiation cooling rates at the two equilibrium temperatures, $\mathcal{T}_1 / \tau_{rad}$ and $\mathcal{T}_2 / \tau_{rad}$ (solid lines).

and assume that $\delta \mathcal{T}_i$ and $\delta \mathcal{D}_i$ vary like $\exp(\lambda_i t)$. To first order in $\delta \mathcal{T}_i$ and $\delta \mathcal{D}_i$, Eqs. (9) and (10) are

$$\lambda_i \delta \mathcal{T}_i = \left(\gamma_i' \mathcal{D}_i - \frac{1}{\tau_{rad}} \right) \delta \mathcal{T}_i + \gamma(\mathcal{T}_i) \delta \mathcal{D}_i,$$

$$\lambda_i \delta \mathcal{D}_i = -(2\gamma_i' \mathcal{D}_i) \delta \mathcal{T}_i + 2(\beta - \gamma(T_i)) \delta \mathcal{D}_i, \qquad (11)$$

where

$$\gamma_i' \equiv \left. \frac{\partial \gamma}{\partial \mathcal{T}} \right|_{\mathcal{T}_i}.$$

Inserting $\mathcal{T}_0 = \mathcal{D}_0 = 0$ and solving for λ_0 gives

$$\lambda_0 = 2(\beta - \gamma(0)). \qquad (12)$$

Inserting $(\mathcal{T}_i, \mathcal{D}_i)$ and solving for λ_i, $i = 1, 2$, gives

$$\lambda_i = \frac{1}{2} \left[\left(\gamma_i' \mathcal{D}_i - \frac{1}{\tau_{rad}} \right) \pm \sqrt{ \left(\gamma_i' \mathcal{D}_i - \frac{1}{\tau_{rad}} \right)^2 - 8\gamma' \beta \mathcal{D}_i } \right].$$
$$(13)$$

A fixed point is unstable if $\lambda_i > 0$. Thus, the low temperature $\mathcal{T}_0 = \mathcal{D}_0 = 0$ fixed point is always unstable for any nontrivial values of resistive destabilization from Eq. (12), i.e. for all $\beta > \gamma(\mathcal{T} = 0)$. Equation (13) shows that the other 2 fixed points are stable only if two conditions are met: $\gamma_i' > 0$ and $\gamma_i' \mathcal{D}_i < 1/\tau_{rad}$.

The condition $\gamma_i' > 0$ must be satisfied for the fixed point to be stable to fluctuations in $\mathcal{D}$. Physically, this means that the slope of the damping rate γ with respect to $\mathcal{T}$ must be greater than the slope of the resistive growth rate β. From Fig. 9 we see that the $(\mathcal{T}_2, \mathcal{D}_2)$ fixed point never satisfies this condition and is always unstable. A small decrease in $\mathcal{D}$ below $\mathcal{D}_2$ decreases the heating rate $\gamma\mathcal{D}$ and thus decreases $\mathcal{T}$. Decreasing $\mathcal{T}$ increases γ, thus causing a further unstable decrease in $\mathcal{D}$. Similarly, a small increase in $\mathcal{D}$ will cause it to unstably grow.

Since $(\mathcal{T}_0, \mathcal{D}_0)$ and $(\mathcal{T}_2, \mathcal{D}_2)$ are both unstable, a plasma with an initial displacement in the range $0 < \mathcal{D}(t = 0) < \mathcal{D}_2$ will have its long term behavior determined by the middle fixed point $(\mathcal{T}_1, \mathcal{D}_1)$. (This condition is satisfied in most of the experiments.) The middle fixed point is always stable to fluctuations in $\mathcal{D}$, but not necessarily stable to fluctuations in $\mathcal{T}$.

The condition for $\mathcal{T}$ stability is $\gamma_i' \mathcal{D}_i < 1/\tau_{rad}$. Physically, this means that the slope of the Joule-heating rate $\gamma\mathcal{D}$ with respect to $\mathcal{T}$ must be less than the slope of the cyclotron radiation cooling rate $\mathcal{T}/\tau_{rad}$. Figure 11(a) shows the heating and cooling rates plotted versus $\mathcal{T}$ for a case where $(\mathcal{T}_1, \mathcal{D}_1)$ is stable. The cooling rate increases faster with $\mathcal{T}$ than the heating rate, so a small increase (decrease) in $\mathcal{T}$ causes increased cooling (heating), which returns $\mathcal{T}$ to $\mathcal{T}_1$. We define $\mathcal{T}_{crit}$ as the "critical" temperature at which the heating and cooling rates have the same slope. Figure 11(b) shows a case where $\mathcal{T}_1 < \mathcal{T}_{crit}$ and the $(\mathcal{T}_1, \mathcal{D}_1)$ fixed point is unstable to temperature fluctuations. Note that the characteristic growth rate for this instability is τ_{rad}^{-1}. This is usually much faster than the characteristic growth rate β around the $(\mathcal{T}_2, \mathcal{D}_2)$ fixed point (which is unstable to $\mathcal{D}$ fluctuations but not $\mathcal{T}$ fluctuations).
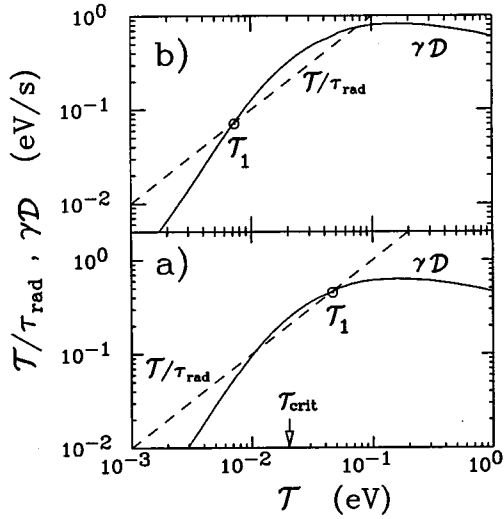
FIG. 11. Stability of the equilibrium temperature $\mathcal{T}_1$ to temperature fluctuations. (a) Stable: $\mathcal{T}_1 > \mathcal{T}_{\text{crit}}$. The slope of the cooling rate $\mathcal{T}/\tau_{\text{rad}}$ is steeper than that of the heating rate $\gamma(\mathcal{T})\mathcal{D}$ at $\mathcal{T} = \mathcal{T}_1$. (b) Unstable: $\mathcal{T}_1 < \mathcal{T}_{\text{crit}}$.

The $(\mathcal{T}_1, \mathcal{D}_1)$ fixed point is unstable ($\mathcal{T}_1 < \mathcal{T}_{\text{crit}}$) only for large enough R_p. Examining Eq. (4) shows that $\mathcal{T}_{\text{crit}}$ is the temperature where $d\nu_{\perp\parallel}/d\mathcal{T} = 0$ (for $T_{\min} \ll \mathcal{T}_{\text{crit}}$); hence $\mathcal{T}_{\text{crit}}$ depends only on the magnetic field. However, $\mathcal{T}_1$ depends on R_p through γ, since $\gamma \propto R_p^2$. Examining Fig. 9, we see that $\mathcal{T}_1$ decreases as R_p increases, making the $(\mathcal{T}_1, \mathcal{D}_1)$ fixed point unstable at large R_p.

The behavior of D and T from 0 to 65 s in Fig. 8 is consistent with the behavior of $\mathcal{D}$ and $\mathcal{T}$ around a stable $(\mathcal{T}_1, \mathcal{D}_1)$ fixed point. D and T diverge away from the (0,0) fixed point after the initial cooling. By 20 s, D and T have overshot (T_1, D_1) and start to diverge from (T_2, D_2). Finally, by 35 s, D and T reach the stable (T_1, D_1) fixed point.

That D and T are stable from 35 to 65 s is evident from the fact that they change at rates slow compared to both β and $1/\tau_{\text{rad}}$. The slow increase in the ratio D/T arises from the slow increase in R_p due to rotational pumping and anomalous transport. The predator-and-prey model predicts that $\mathcal{D}_1/\mathcal{T}_1 = 1/\beta\tau_{\text{rad}}$. Converting to the physical variables shows that D_1^2/T_1 should grow nearly linearly with R_p^2:

$$\frac{(D_1/R_w)^2}{(T_1 - T_{\min})} = \frac{(R_p/R_w)^2}{\frac{4}{3}N_L e^2 (1 - (R_p/R_w)^2)\beta\tau_{\text{rad}}}. \tag{14}$$

Equation (14) is in close agreement with the model evolution of Fig. 8. The unstable drop in T at 65 s, accompanied by a Hopf bifurcation[6] into sawtooth oscillations, is also consistent with the model's prediction that the temperature should go unstable when R_p becomes large enough that T_1 falls below T_{crit}. Finally, since the model evolution of Fig. 8 is in qualitative agreement with the measured evolution of Fig. 4, which it was meant to simulate, we believe the model agrees with the data in Fig. 4 as well.

C. Small oscillations

Equation (12) shows that λ_i is complex if $(\gamma_i' \mathcal{D}_i - 1/\tau_{\text{rad}})^2 < 8\gamma_i'\beta\mathcal{D}_i$. This condition is satisfied only if $\gamma_i' > 0$, i.e. only at the $(\mathcal{T}_1, \mathcal{D}_1)$ fixed point, and only if the real part of λ_i is small compared to the imaginary part, which occurs when $\mathcal{T}_1 \approx \mathcal{T}_{\text{crit}}$. If these conditions are satisfied, $\delta\mathcal{T}_1$ and $\delta\mathcal{D}_1$ will execute small oscillations. The oscillations grow or damp at the rate $(\gamma_i'\mathcal{D}_i - 1/\tau_{\text{rad}})/2$. At marginal stability, $\gamma_i'\mathcal{D}_1 = 1/\tau_{\text{rad}}$ and λ_1 is purely imaginary. In this case, the oscillation frequency is

$$\text{Im}(\lambda_1) = \sqrt{2\beta/\tau_{\text{rad}}},$$

and $\delta\mathcal{D}_1$ and $\delta\mathcal{T}_1$ are related by

$$\frac{\delta\mathcal{D}_1}{\mathcal{D}_1} = e^{i(\pi/2)}\sqrt{2\beta\tau_{\text{rad}}}\frac{\delta\mathcal{T}_1}{\mathcal{T}_1}. \tag{15}$$

The measured sinusoidal oscillations of D and T shown in Fig. 6 are in good quantitative agreement with the small oscillations around the $(\mathcal{T}_1, \mathcal{D}_1)$ fixed point predicted by the model. Since the oscillations are weakly damped, the fixed point must be near marginal stability, with $\mathcal{T} \approx \mathcal{T}_{\text{crit}}$. The measured oscillation period, 8.5 s, is within 5% of the predicted frequency at marginal stability, $\sqrt{2\beta/\tau_{\text{rad}}}$. The measured relative amplitudes of the T and D oscillations, $\delta\mathcal{D}/\mathcal{D}_1$ and $\delta\mathcal{T}/\mathcal{T}_1$, and the phase difference between them, $\pi/2$, are within 15% of the prediction of Eq. (15). Furthermore, the measured values of the average T and D are within 20% of the predicted values of T_1, D_1. The quantitative discrepancies between the model and the measurements are smaller than the experimental uncertainty. Due to the poor resolution of the radial density profile measurements, the long confinement times, and the complexity of the evolutions of D and T, we estimate a 20% uncertainty in measuring $\mathcal{D}$ and at least 10% in $\mathcal{T}$.

D. Limit cycles

Even if the $(\mathcal{T}_1, \mathcal{D}_1)$ fixed point is unstable, $\mathcal{T}$ and $\mathcal{D}$ do not diverge from it without bound. Instead, they execute limit cycles[6] around the unstable fixed point. These limit cycles correspond to the sawtooth oscillations of D and T shown in Figs. 4, 5, 7, and 8.

Most of the time, the plasma temperature is determined by a balance between heating and cooling. This occurs because $\beta\tau_{\text{rad}} \ll 1$. That is, the temperature is able to respond quickly to changes in the displacement. In this limit, the evolution of $\mathcal{T}$ can be described by setting the heating term equal to the cooling term in Eq. (9), i.e. $\mathcal{T} = \mathcal{T}_*$, where

$$\frac{\mathcal{T}_*}{\tau_{\text{rad}}} = \gamma(\mathcal{T}_*)\mathcal{D}. \tag{16}$$

We determine the stability of this quasi-equilibrium temperature by setting $\mathcal{D}_i = \mathcal{D}$, $\mathcal{T}_i = \mathcal{T}_*$, and $\delta\mathcal{D}_i = 0$ in Eq. (11). The quasi-equilibrium is stable to temperature fluctuations as long as $(d\gamma/d\mathcal{T})|_{\mathcal{T}_*}\mathcal{D} < 1/\tau_{\text{rad}}$, which is the same criterion as was determined in Sec. V B for the fixed points. Note that in Eq. (16), as $\mathcal{T}_*$ approaches 0, $\gamma(\mathcal{T}_*)$ does *not* go to zero (for nonzero $T_{\min}$). Hence $\mathcal{D}$ must go to zero at $\mathcal{T}_* = 0$, and the stability condition holds at small enough $\mathcal{T}$.
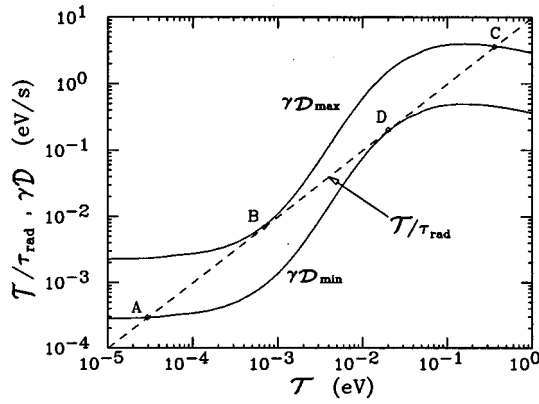
Cluggish *et al.*

FIG. 12. Changes in $\mathscr{D}$ and $\mathscr{T}$ during a limit cycle. The cooling rate (dashed line) depends only on $\mathscr{T}$. The heating rate depends on both $\mathscr{T}$ and $\mathscr{D}$; the solid lines show the heating rate at the maximum and minimum values of $\mathscr{D}$ during the limit cycle.

When $\mathscr{T}$ is unstable, it rapidly diverges from $\mathscr{T}_*$, at a characteristic rate of $1/\tau_{\text{rad}}$. However, $\mathscr{T}_*$ is multi-valued for $\mathscr{D}$ near $\mathscr{D}_1$ due to the nonmonotonic dependence of γ on $\mathscr{T}$ and due to $T_{\min}$ being greater than zero. Thus, any unstable $\mathscr{T}_*$ is bounded below by the stable region near $\mathscr{T}=0$ and above by the stable region where $d\gamma/d\mathscr{T}\leqslant 0$; this limits the magnitude of unstable excursions. The range of $\mathscr{D}$ is likewise bounded, as can be seen by differentiating Eq. (16) with respect to $\mathscr{T}_*$, i.e.

$$\frac{d\mathscr{D}}{d\mathscr{T}_*}=\frac{1}{\gamma}\left(\frac{1}{\tau_{\text{rad}}}-\frac{d\gamma}{d\mathscr{T}_*}\mathscr{D}\right).$$

The maximum and minimum values of $\mathscr{D}$ occur at marginally stable values of $\mathscr{T}_*$, i.e. where $(d\gamma/d\mathscr{T}_*)\mathscr{D}=1/\tau_{\text{rad}}$. These stability boundaries give rise to limit cycles of $\mathscr{D}$ and $\mathscr{T}$.

Figure 12 shows the heating rate $\gamma\mathscr{D}$ and cooling rate $\mathscr{T}/\tau_{\text{rad}}$ plotted versus temperature. The dashed line is $\mathscr{T}/\tau_{\text{rad}}$, while the two solid curves are the heating rates at $\mathscr{D}_{\max}$ and $\mathscr{D}_{\min}$, the maximum and minimum values of $\mathscr{D}$ during the limit cycle. The limit cycle evolves through A, B, C, D in Fig. 12; the equivalent points are also shown as A, B, C, D in Fig. 5. The limit cycle starts at point A, where both $\mathscr{T}=\mathscr{T}_*$ and $\mathscr{D}$ are minimum. Since $(d\gamma/d\mathscr{T})\mathscr{D}<1/\tau_{\text{rad}}$ at this point, $\mathscr{T}_*$ is stable. However, $\mathscr{D}$ increases slowly because $\beta>\gamma$ for $\mathscr{T}<\mathscr{T}_1$; this causes $\mathscr{T}_*$ and $\gamma\mathscr{D}$ to increase as well. Eventually, $\gamma\mathscr{D}$ becomes so large that heating overwhelms cooling. This occurs at point B; $\mathscr{T}_*$ becomes unstable and $\mathscr{T}$ and $\gamma\mathscr{D}$ rapidly grow (at a rate much faster than β) until the stable $\mathscr{T}_*$ at point C is reached. Now β is less than γ, and D slowly decreases, causing $\mathscr{T}_*$ and $\gamma\mathscr{D}$ to decrease as well. At point D, cyclotron cooling becomes dominant, making $\mathscr{T}_*$ unstable. $\mathscr{T}$ and $\gamma\mathscr{D}$ then rapidly drop to point A, where the cycle begins again.

The measured sawtooth oscillations of D and T shown in Fig. 5 are in good structural agreement with the limit cycles predicted by the model. Compared to Fig. 12, we see that the exponential increase in D during the sawtooth rise, where T is small and nearly constant, corresponds to the

$A\rightarrow B$ portion of the limit cycle, whereas the factor of 60 rapid increase in T at the maximum D corresponds to the jump from B to C. The decrease in T and D over the next 4 s ($\gg\tau_{\text{rad}}$) is consistent with the $C\rightarrow D$ portion of the cycle. Finally, the rapid drop in T from 0.025 eV to 0.004 eV at the minimum D is consistent with the jump from D to A.

In the limits $\beta\tau_{\text{rad}}\ll 1$ and $\mathscr{T}_1\gg T_{\min}$, simple relationships can be derived between the rise time, crash time, and amplitude of the sawteeth. We assume that D increases (decreases) exponentially during each sawtooth rise (crash). During the sawtooth rise, $\beta\gg\gamma$, so the rise time is given by

$$t_{\text{rise}}=\frac{1}{\beta}\ln\left(\frac{D_{\max}}{D_{\min}}\right).$$

During the sawtooth crash, $\gamma>\beta$. To estimate γ, we note that during most of the sawtooth crash shown in Fig. 5, the temperature remains near the temperature corresponding to the peak of the plot of γ in Fig. 1. Since the dependence of γ on temperature is weak near the peak, we can approximate γ during the sawtooth crash by $\gamma\approx\gamma_{\text{peak}}$, where γ_{peak} is the value of γ at the peak. Then the crash time is given by

$$t_{\text{crash}}=\frac{1}{\gamma_{\text{peak}}-\beta}\ln\left(\frac{D_{\max}}{D_{\min}}\right).$$

Using Eqs. (3) and (4) to calculate β and γ_{peak} from the experimental parameters for the data in Fig. 5, we calculate a rise time about 40% shorter than the measured time of 15.2 s, and a crash time about 20% shorter than the measured time of 4.6 s. The source of the error is most likely the shortcomings of Eqs. (3) and (4). The equation for β assumes a long plasma ($L_p\gg R_w$), and the equation for γ assumes a uniform radial density profile. Neither of these assumptions holds in the experiment.

E. Bifurcation

The model predicts that the $(\mathscr{T}_1,\mathscr{D}_1)$ fixed point is stable only for small enough R_p. In the experiments, R_p slowly increases due to rotational pumping and anomalous transport. As shown in Fig. 8, T_1 decreases as R_p increases. When T_1 falls below T_{crit}, the fixed point becomes unstable and the system undergoes a Hopf bifurcation into limit cycles (sawtooth oscillations). The limit cycles may be preceded by small oscillations. For example, in Fig. 7, the small oscillations grow for 3 cycles before turning into limit cycles. In Fig. 4, on the other hand, no precursor oscillations are observed. This indicates that R_p is increasing so rapidly that λ_1 is complex for less than one oscillation period.

VII. TIME-DEPENDENT ANOMALOUS TRANSPORT

In the model evolution depicted in Fig. 8, we assumed a constant value for the anomalous transport rate ϵ. Although the agreement between the model and the data in Fig. 4 is fairly good, there are some discrepancies. In this section we show that these discrepancies can probably be resolved by using a more accurate model for ϵ.
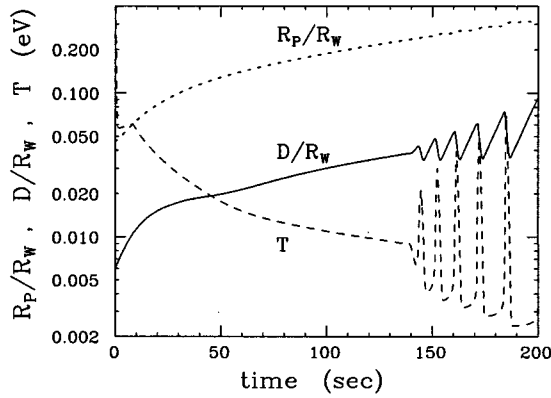
FIG. 13. Model evolution of D, T, and R_p obtained using a temperature and density dependent anomalous transport rate [Eq. (17)] in the numerical integration of Eqs. (5)–(7). Initial conditions are the same as the measured evolution shown in Fig. 4 and the simulated evolution shown in Fig. 8. The measured evolution shown in Fig. 4 shares features of both simulations.

In Fig. 13 we show the evolution of D, T, and R_p obtained by numerically integrating Eqs. (5)–(7) starting from the same initial conditions as Figs. 4 and 8, but using the following model for ϵ:

$$\epsilon = 0.03 \left(\frac{f_R}{f_B} \right)^2 \propto R_p^{-2} T^{-1}. \qquad (17)$$

This is an empirical estimate for ϵ which approximates the measured scalings with R_p and T, and correctly predicts the plasma lifetime within an order of magnitude.[16]

Comparison of Figs. 8 and 13 shows that the basic features of the observed evolution are independent of the model for ϵ. Both simulations show initial linear growth to a stable equilibrium, and then a bifurcation into limit cycles, with quantitative agreement with the measured evolution of D to within a factor of 2. This similarity between the two simulations occurs because, in both models, ϵ is small and does not increase with T. This means that heating from anomalous transport is insignificant compared to heating from rotational pumping except at the lowest temperatures. It also means that both models for ϵ define a minimum temperature to which the plasma can cool, i.e.

$$T_{\min} = \frac{2}{3} N_L e^2 \epsilon(R_p, T_{\min}) \tau_{\rm rad} + T_w.$$

This equation is the same as Eq. (8), except for the dependence of ϵ on R_p and T. $T_{\min}$ decreases as R_p increases with time, since the empirical model for ϵ decreases with R_p.

The differences between the simulations of Figs. 8 and 13 indicate that anomalous transport is responsible for some of the discrepancies between the simulations and the data in Fig. 4. First, both Fig. 4 and Fig. 13 show a monotonic increase in D for the first 100 s, whereas Fig. 8 shows a peak at 20 s. This indicates that the actual plasma temperature did not undergo a large oscillation as shown in Fig. 8. Rather, the initial value of the actual anomalous transport rate was so large that the initial $T_{\min} \approx 0.06$eV was larger than $T_{\rm crit}$, stabilizing the temperature against rapid cooling. As R_p slowly

increased, ϵ and $T_{\min}$ slowly decreased, causing $T(D)$ to monotonically decrease (increase), as shown in Fig. 13.

A second feature of the evolution which depends on anomalous transport is the time at which the bifurcation into sawtooth oscillations occurs. In the simulation of Fig. 8, this bifurcation occurs 30 s earlier than measured bifurcation time in Fig. 4; in the simulation of Fig. 13, it occurs 30 s later. This discrepancy arises because $T_{\rm crit}$ increases as $T_{\min}$ decreases. Thus, the smaller the anomalous transport rate, the earlier the bifurcation occurs.

A third feature of the evolution which is sensitive to anomalous transport is the amplitude of the sawtooth oscillations. In the simulation of Fig. 8, ϵ and $T_{\min}$ are defined to be constant, and the amplitude of the sawteeth changes only slightly. In Fig. 13, ϵ and $T_{\min}$ decrease with time, causing the oscillation amplitude to grow. The measured evolution of Fig. 4 is somewhere in between the 2 simulations, indicating that a more accurate model for the anomalous transport rate would probably give better agreement between simulation and experiment.

The strong increase in sawtooth amplitude with decreasing $T_{\min}$ in Fig. 13 illustrates an important role which anomalous transport plays in the nonlinear interaction between D and T. That is, a nonzero $T_{\min}$ limits the maximum value to which D can grow. In fact, without anomalous transport, D would simply grow until the plasma hit the wall; for $T_{\min} = T_w = 3.7 \times 10^{-4}$ eV (4.2 K), the maximum D is greater than R_w.

VIII. FURTHER PREDICTIONS OF THE MODEL

In this section we discuss two further predictions of the predator-and-prey model. One is unstable growth of T and D when $\mathscr{D} > \mathscr{D}_2$; this does not usually occur because R_p increases rapidly, violating the assumption of the model. The other prediction is stabilization of the $(\mathscr{T}_1, \mathscr{D}_1)$ fixed point at very low temperatures and large R_p; this has not been observed.

The predator-and-prey model predicts that $\mathscr{T}$ and $\mathscr{D}$ will increase without bound for $\mathscr{D} > \mathscr{D}_2$, because the $(\mathscr{T}_2, \mathscr{D}_2)$ fixed point is always unstable to fluctuations in D. (The instability arises because $d\gamma/d\mathscr{T} < 0$ at $\mathscr{T}_2$, as shown in Fig. 9.) This unphysical behavior does not occur in the experiments because dR_p/dt increases as D increases. Increasing R_p increases $\mathscr{T}_2$ and $\mathscr{D}_2$. Eventually R_p becomes so large that $\mathscr{T}_2$ and $\mathscr{D}_2$ overtake $\mathscr{T}$ and $\mathscr{D}$. Then $\mathscr{D}$ is less than $\mathscr{D}_2$, and $\mathscr{T}$ and $\mathscr{D}$ decrease away from the unstable $(\mathscr{T}_2, \mathscr{D}_2)$ fixed point.

Figure 14 shows a measured example of this behavior. The plasma is hot ($T > 1$ eV) upon injection, but rapidly cools. At 3.7 s, we move the plasma off-axis to $D/R_w = 0.055$. The subsequent heating causes the temperature to jump up a factor of 5 in 0.1 s, until T reaches a quasi-equilibrium T_* given by Eq. (16). For about 0.8 s thereafter, the temperature continues to grow, but at a rate about 50 times slower, $(1/T)(dT/dt) \approx 0.3$ s$^{-1} \ll 1/\tau_{\rm rad}$. The simultaneous growth of D during this time indicates that $\mathscr{T}$ and $\mathscr{D}$ are diverging away from $(\mathscr{T}_2, \mathscr{D}_2)$. This unstable behavior is short lived, however. The plasma radius R_p rapidly
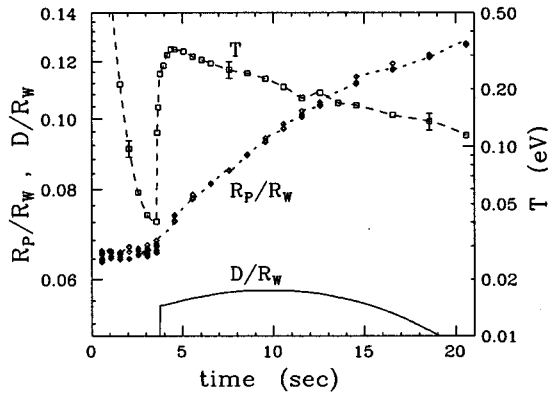
Cluggish *et al.*

FIG. 14. Instability of $(\mathcal{T}_2, \mathcal{D}_2)$. From 3.7 to 4.5 s, both T and D grow at a rate slow compared to $1/\tau_{\mathrm{rad}}$, indicating that they are unstably diverging from $(\mathcal{T}_2, \mathcal{D}_2)$. The rapid growth of R_p moves the fixed point $(\mathcal{T}_2, \mathcal{D}_2)$ above T and D, so that after 10 s both T and D are unstably decreasing toward $(\mathcal{T}_1, \mathcal{D}_1)$.

increases; by 4.5 s T starts to decrease, and by 10 s D is decreasing as well towards the $(\mathcal{T}_1, \mathcal{D}_1)$ fixed point.

The fact that T and D are not maximum at the same time is a consequence of the rapid change in R_p. Since $\beta\tau_{\mathrm{rad}} \ll 1$, the relationship between T and D is set by Eq. (16). Differentiating Eq. (16) with respect to time and converting to the physical variables gives

$$\frac{1}{D^2}\frac{dD^2}{dt} = \left[\frac{1}{R_p}\frac{dR_p}{dt} + \left(1 - \frac{T}{\gamma}\frac{d\gamma}{dT}\right)\frac{1}{T}\frac{dT}{dt}\right]_{T=T_*},$$

where we have used Eq. (4) for γ. Since $d\gamma/dT < 0$ for $\mathcal{T} \gtrsim \mathcal{T}_2$ and $dR_p/dt > 0$, the temperature must be decreasing when D is maximum, in agreement with Fig. 14.

The unobserved second prediction of the model is that the $(\mathcal{T}_1, \mathcal{D}_1)$ fixed point should be stable for very small $\mathcal{T}$, i.e. $\mathcal{T}$ less than the temperature of point B in Fig. 12. This condition should occur for very large R_p, where $\gamma > \beta$ except at the very lowest temperatures. However, we have not observed this stabilization of $\mathcal{T}_1$ at large R_p, probably because the plasma is not uniform in density as the model assumes. Measurements of the radial density profile indicate that the density profile has low density ''wings'' extending far from the bulk of the plasma. Presumably, these wings contact the trap walls before γ can become large enough for $\mathcal{T}_1$ to be stabilized. For instance, in the evolution shown in Fig. 4, the plasma starts losing electrons to the wall at 275 s, even though $R_p + D < R_w$. Surprisingly, contact with the wall has little effect on the plasma behavior; the sawtooth oscillations last for hundreds of seconds longer.

IX. CONCLUSIONS

We have made measurements of a nonlinear evolution of the displacement of a pure electron plasma column in a cy-lindrical trap. The evolution occurs when the displacement is destabilized by a resistive wall and damped by temperature-dependent rotational pumping. Our measurements show that oscillations of the displacement, D, are coupled to oscillations of the temperature, T, and are accompanied by a monotonic increase in the plasma radius, R_p. Quantitative agreement of the data with numerical integration of model evolution equations indicates that the coupling between D, T, and R_p arises through rotational pumping transport.

In the limit where R_p changes only slowly, the model equations reduce to a pair of predator-and-prey type equations for D and T, where R_p is a control parameter. Fixed points for this system exist where resistive growth is balanced by rotational pumping damping, and Joule-heating from the transport is balanced by cyclotron radiation cooling. The location of the fixed points depends on R_p. Nonlinear behavior arises because the stability of the fixed points is determined by the dependence of the transport rate on temperature, and that dependence is nonmonotonic. Thus, at large enough R_p, a stable equilibrium can become unstable. This leads to bifurcation into limit cycles around the unstable fixed point, corresponding to the observed sawtooth oscillations.

[1] F. A. Haas and A. Thyagaraja, Plasma Phys. Controlled Fusion **37**, 415 (1995).
[2] W. W. Heidbrink and J. R. Danielson, Phys. Plasmas **1**, 4120 (1994).
[3] V. B. Lebedev, P. H. Diamond, I. Gruzinov, and B. A. Carreras, Phys. Plasmas **2**, 3345 (1995).
[4] R. Schrittwieser, Phys. Fluids **26**, 2250 (1983); S. Ilzuka, P. Michelson, J. J. Rasmussen, R. Schrittwieser, R. Hatakeyama, K. Saeki, and N. Sato, Phys. Rev. Lett. **48**, 145 (1982).
[5] T. Gyergyek, M. Cercek, M. Stanojevic, and N. Jelic, J. Phys. D Appl. Phys. **27**, 2080 (1994).
[6] R. C. Hilborn, *Chaos and Nonlinear Dynamics: An Introduction for Scientists and Engineers* (Oxford University Press, New York, 1994).
[7] J. Helffrich, B. R. Beck, B. Cluggish, J. M. Fajans, and J. H. Malmberg, Bull. Am. Phys. Soc. **35**, 2135 (1990).
[8] B. P. Cluggish and C. F. Driscoll, Phys. Plasmas **3**, 1813 (1996).
[9] B. R. Beck, Ph.D. dissertation, University of California, San Diego, 1990.
[10] B. P. Cluggish, Ph.D. dissertation, University of California, San Diego, 1995.
[11] K. S. Fine, Phys. Fluids B **4**, 3981 (1992).
[12] K. S. Fine, Ph.D. dissertation, University of California, San Diego, 1988.
[13] W. D. White, J. H. Malmberg, and C. F. Driscoll, Phys. Rev. Lett. **49**, 1822 (1982).
[14] S. Crooks and T. M. O'Neil, Phys. Plasmas **2**, 355 (1994).
[15] C. F. Driscoll, K. S. Fine, and J. H. Malmberg, Phys. Fluids **29**, 2015 (1986).
[16] A. C. Cass, B. P. Cluggish, F. Anderegg, K. S. Fine, C. F. Driscoll, and E. Sarid, Bull. Am. Phys. Soc. **39**, 1737 (1994).